Nuclear Instruments and Methods in Physics Research A 605 (2009) 215–223

Contents lists available at ScienceDirect

Nuclear Instruments and Methods in Physics Research A

journal homepage: www.elsevier.com/locate/nima

RF photo-injector beam energy distribution studies by slicing technique

D. Filippetto [a,*], M. Bellaveglia [a], P. Musumeci [b], C. Ronsivalle [c]

[a] INFN-LNF, Via E. Fermi 40, Frascati, Rome, Italy
[b] UCLA-Department of Physics and Astronomy, 405 Hilgard Avenue, Los Angeles, CA 90095, USA
[c] ENEA, Via E. Fermi, 00044 Frascati, Rome, Italy

ARTICLE INFO

Article history:
Received 13 March 2009
Accepted 16 March 2009
Available online 7 April 2009

Keywords:
Energy
Energy spread
Slit
Emittance-meter
Trace space
Phase space
Longitudinal-transverse correlation
Energy distribution
SPARC
Photo-injector
Longitudinal space charge

ABSTRACT

The SPARC photo-injector is an *R&D* facility dedicated to the production of high brightness electron beams for radiation generation via FEL or Thomson scattering processes. It is the prototype injector for the recently approved SPARX project, aiming at the construction in the Frascati/University of Rome Tor Vergata area of a new high brightness electron linac for the generation of SASE-FEL radiation in the 1–10 nm wavelength range. The first phase of the SPARC project has been dedicated to the e-beam source characterization; the beam transverse and longitudinal parameters at the exit of the gun have been measured, and the photo-injector settings optimized to achieve best performance. Several beam dynamics topics have been experimentally studied in this first phase of operation, as, for example, the effect of photocathode driver laser beam shaping and the evolution of the beam transverse emittance. These studies have been made possible by the use of a novel diagnostic tool, the "*emittance-meter*" which enables the measurement of the transverse beam parameters at different positions along the propagation axis in the very interesting region at the exit of the RF gun. The new idea of extending the e-meter capabilities came out more recently. Information on the beam longitudinal phase space and correlations with the transverse planes can be retrieved by the slicing technique. In this paper, we illustrate the basic concept of the measurement together with simulations that theoretically validate the methodology. Some preliminary results are discussed and explained with the aid of code simulations.

1. Introduction

The generation of high brightness beams by RF photo-injectors is a key step enabling many novel and advanced electron beam applications like SASE-FELs [1–3], inverse Compton scattering [4], ultrafast relativistic electron diffraction [5], etc. While the physics of high brightness beam sources has been described in detail [6–8], we observe that much of the attention theoretically and experimentally has been given to the evolution of the transverse beam parameters (in particular beam sizes and normalized emittances) in the initial space charge dominated regime. Even though the beam energy distribution does not appear directly in the definition of the beam brightness which is $B = 2I/\varepsilon_n^2$, it is undeniable that for the beam applications (as, e.g., the free-electron laser) the control of the beam spectrum is as important as the other dimensions of the beam six-dimensional phase space. Just as the transverse dynamics is dominated by a complicate interplay between the external focusing forces and the space charge forces, the beam energy spread results from the different contributions of external RF accelerating fields and the beam self-fields. In particular the energy spread shares with the transverse emittance the property that it is preserved in a drift when space charge effects are negligible. Henceforth, studying the behaviour of this parameter in the space charge dominated region at low energy immediately outside the RF gun offers a complementary point of view in understanding the complex dynamics of high brightness beams. In this paper we present a method of measuring the evolution of the beam energy distribution, based on intercepting the beam with a slit to effectively freeze its momentum space at different positions along the beamline and then retrieving its spectrum with a magnetic spectrometer. First tests of this technique have been carried in the same experimental facility—the SPARC photo-injector—where recently the theoretically predicted emittance oscillations [9] in the drift region following the gun have been characterized [10].

2. Experimental layout

A picture of the SPARC first phase experimental layout is shown in Fig. 1. It consists of a standard UCLA/SLAC/BNL 1.6 cell S-band gun (working at 2.856 GHz), operating at a peak accelerating gradient of 120 MV/m, followed by a solenoid lens composed by

E-mail address: Daniele.Filippetto@lnf.infn.it (D. Filippetto).

0168-9002/$ - see front matter © 2009 Elsevier B.V. All rights reserved.
doi:10.1016/j.nima.2009.03.234

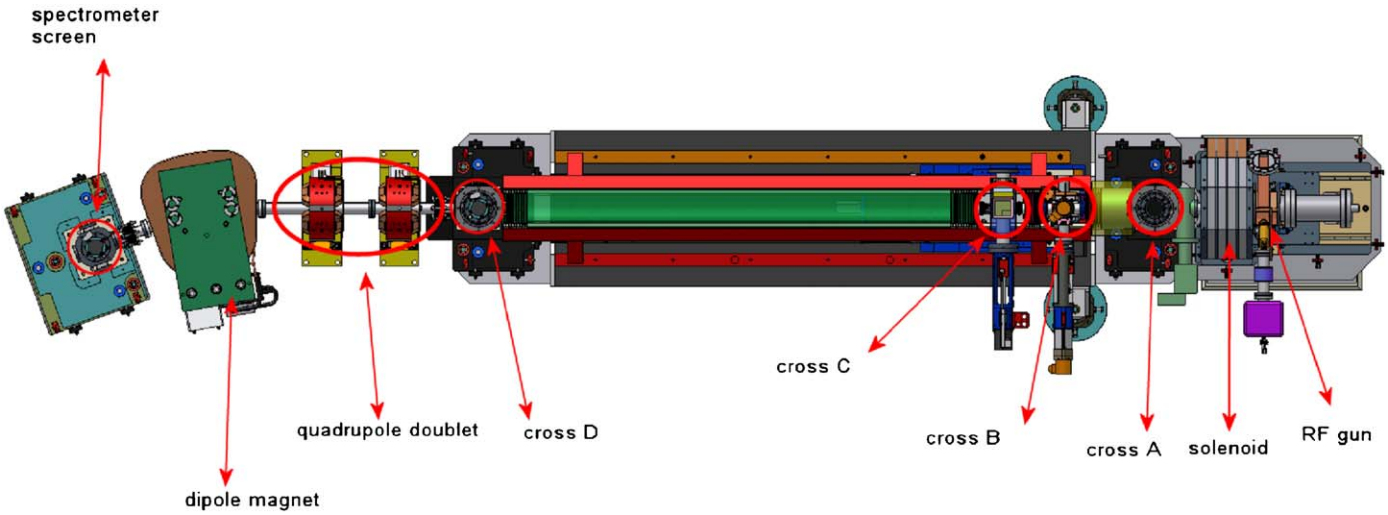

Fig. 1. Schematic layout of SPARC phase 0 experiment.

four independently powered coils. A UV laser beam hits the copper cathode placed on the first half cell of the photo-injector gun and produces the electron bunch. The laser beam is created by a TW-class *Ti* : *Sapphire* system manufactured by Coherent Inc. The 100 fs infrared pulse out of the *Ti* : *Sapphire* oscillator is amplified and then frequency-multiplied in harmonic generation crystals. A shaping system in the *UV* can create a flat-top longitudinal profile with very short (<2 ps) rise-time [11], and change the pulse length (1–10 ps). The diagnostic cross after the solenoid (A in Fig. 1) houses a fluorescent screen used as a first monitor of the beam out of the gun (in particular for centering the laser beam on the cathode). The two following diagnostic crosses (B and C) are used for beam measurements and their position along the beamline can be changed by about 1.2 m compressing and stretching the three bellows that connect them with the rest of the machine. Cross B hosts two orthogonally mounted actuators that can insert in the beam path an horizontal or a vertical slit mask via high precision microstep motors. Each mask is formed by a set of seven slits 50 μm wide and 2 mm thick with 50 μm separation (which can be utilized for single shot emittance measurements), plus two single slits, respectively, 100 and 50 μm wide. Cross C contains a *Yag* : *Ce* target also mounted on a remote controlled actuator for beam imaging. Using these two crosses we can measure the evolution of the beam emittance from 80 cm to about 2 m from the cathode plane, hence the name of the device "emittance-meter" [12]. This setup and the results obtained with it have been described in detail elsewhere [13]. At the end of the beamline a quadrupole doublet is used in combination with the following dipole magnet, to measure the energy and energy spread on the last scintillator screen (*Yag* : *Ce*) around the 22° bend. The dispersion plane coincides with the horizontal plane. The simultaneous presence of a spectrometer and a transverse collimator (slit mask) suggests a novel diagnostic technique to study the evolution of the beam energy and energy spread evolution and to unveilcorrelations between the energy and the transverse beam coordinates.

3. The basic concept

In these pages *X*,*Y* and *Z* will be referred, respectively, to the horizontal, vertical and longitudinal coordinates along the accelerator beamline.

In a space charge dominated beam each particle experiences and interacts with the electromagnetic field produced by the surrounding particles. As a consequence the transverse and longitudinal electron momenta cannot be considered constant even in the absence of externally applied fields. The effect of a transverse collimator intercepting the bunch is to suddenly reduce the beam current, effectively zeroing the effect of both transverse and longitudinal self-forces. The original purpose of the collimator in cross B was to minimize the transverse space charge forces for transverse emittance measurements. The aperture width had been chosen as the best compromise between the fraction of residual space charge forces and the number of electrons needed for a good detection and analysis. The electron beam current is typically reduced by at least a 10-fold factor after the cut leading to a strong reduction of longitudinal (as well as transverse) self-forces on the beamlet; as a consequence the beamlet energy spread growth is heavily dumped.

The idea pursued is that of measuring the sliced beamlet energy and energy spread after the propagation until the spectrometer screen. Such a measurement effectively yields information on the energy distribution at the collimator plane. By repeating this measurement for different collimator positions along the propagation axis the energy spread evolution can be followed. Fig. 2 shows a cartoon schematic of the measurement. Furthermore, by moving transversely the collimating slit across the beam one could in principle reconstruct the full $X-E$ ($Y-E$) trace space.

A first simulation run has been dedicated to the evaluation of the systematic error introduced by the residual space charge when measuring the beamlet energy spread after a drift, and not immediately after the collimator. Particle coordinates at the slit plane have been generated with *PARMELA* [15] and a cut on the distribution by a 50 μm single vertical slit has been applied, by excluding the particles outside the aperture. The new file has then been used as input for a new *PARMELA* run. Since the number of particles out of the slit is of the order of few percent (decreasing with the distance of the slit plane from the waist position), the initial number of particles t_0 used in simulation has to be very high ($t_0 = 0.5 \times 10^6$) to have a reasonable resolution. Fig. 3 shows the results of simulations on one of the experimental cases presented in next chapter: an initial laser pulse of 420 μm radius and 5 ps *FWHM* length, with 1 ps rise time, 360 pC charge and $E_0 = 120$ MV/m accelerating gradient in the gun. The injection phase is $\phi_{inj} = 30°$ (corresponding to ϕ_0 of Fig. 4). The three plots

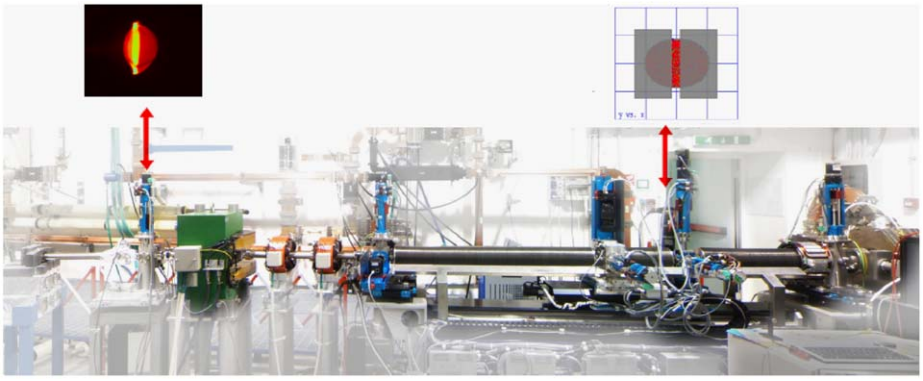

Fig. 2. A cartoon schematic of the idea of measurement. The beam sliced by a collimator at a movable position propagates through a dispersive section until the scintillation screen where the energy and the energy spread are measured.

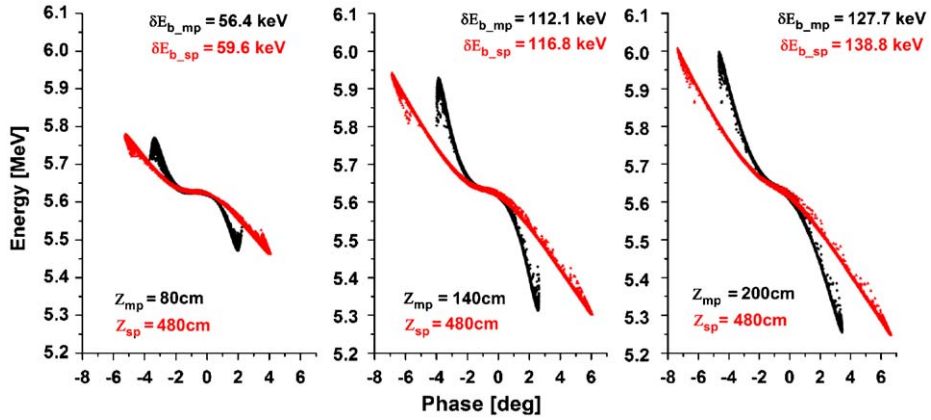

Fig. 3. Comparison between beamlet longitudinal trace spaces at the mask plane (black, δE_{b_mp}) and at the spectrometer screen position (red, δE_{b_sp}), for three different longitudinal positions Z_{mp} 80, 140, and 200 cm. (For interpretation of the references to color in this figure legend, the reader is referred to the web version of this article.)

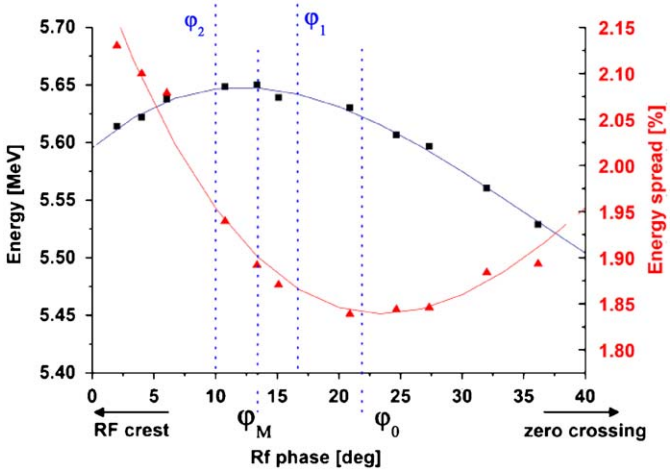

Fig. 4. Typical energy and energy spread scan versus RF phase. The four dotted lines mark the four different phases used in the measurements.

represent the longitudinal beamlet trace space in three different Z positions of collimating mask: 80, 140 and 200 cm from the cathode plane. For any plot black dots refer to the beamlet longitudinal trace space just after the slit cut, while red dots refer to the same beam after the propagation until the spectrometer screen (480 cm from cathode plane). The time duration of the pulse increases along the drift (horizontal axis), due to the energy chirp accumulated by the beam before the slit. The RMS energy spread of each beamlet has been calculated by projecting each trace space on the energy (vertical) axis, and the results are reported in the figure, where δE_{b_mp} and δE_{b_sp} are, respectively, the RMS beamlet energy spread at the mask plane and at the spectrometer plane.

The difference between δE_{b_mp} and δE_{b_sp} leads to a systematic error that is always less or equal to 5%.

In what follows a first test of beamlet energy distribution measurement is presented.

These measurements do not show the full $X-E$ plane, but the evolution of the central beam slice with the distance from cathode. Both the RMS energy spread and the complete energy distribution profile have been compared with simulations showing a good agreement.

A complete measurement would imply the measurement and reconstruction of the whole $X-E$ ($Y-E$) plane, but already from these first dataset the feasibility and limitations of such a method can be exploited and understood.

Also we observed correlations between the particle energy and their transverse trace space behavior obtaining, with the aid of simulation codes, an explanation based on the concept of plasma frequency spread (as already theoretically explained by Carlsten [7]).

4. Energy evolution measurements and analysis

The central beamlet energy spread (δE_b) evolution has been measured as a function of beam charge and RF launch phase, and the results are reported in this chapter. The evolution of the energy distribution profile (not only of its second order moment) has been studied for a particular double-peaked laser temporal profile illuminating the cathode (Fig. 8). This particular laser shape has been chosen to make evident the effect of the laser longitudinal distribution to the electron beam energy spectrum.

A complete reconstruction of the entire $X-E$ plane and a precise measurement of the beam energy spread at different longitudinal positions would require to sampling (slicing) the beam at different transverse positions for each Z position.

A critical parameter for the beam dynamics (especially the longitudinal one) is the relative time of arrival of the laser beam on the cathode with respect of the RF accelerating wave. The measurements presented were performed at different RF launch phases. We will always refer to an optimum injection phase (ϕ_0) as the phase of minimum energy spread phase, deviating deviates from the maximum energy phase (ϕ_M) by 8°. Fig. 4 shows the measurements of energy and energy spread as a function of launch phase. The two phases used during the measurements presented in this paper are ϕ_1, separated from ϕ_0 by 5° toward the maximum energy phase (ϕ_M)), and ϕ_2 whose difference from ϕ_0 is 12° in the same direction and lies in fact on the other side of ϕ_M.

Fig. 5 shows the results of central beamlet energy spread δE_b as a function of the 50 μm wide slit collimator in four different experimental situations. We repeated the measurement for two different beam charges (200 and 360 pC) by varying the input laser energy and for two different injection phases (ϕ_0 and ϕ_2). The last point on the curves (4800 mm) represents instead the RMS energy spread of the entire beam (δE_t) on the spectrometer screen. The qualitative behavior of the measured curves is in agreement with the expectations: the energy spread strongly depends on the RF phase and increasing the charge leads to a beam spectrum which is wider and more quickly growing during propagation. The strong dependence on the launch phase is due by the fact that in the case $\phi_{inj} = \phi_0$ the self-fields and the RF field in the gun tend to chirp the electron beam with opposite slopes, resulting in a partial cancelation of their effects and hence a lower energy spread. In case of $\phi_{inj} = \phi_2$ instead the induced chirp has the same sign resulting in a much higher energy spread [14].

Simulations with experimental beam parameters have been carried out to fit the data. In Fig. 6 the comparison between *PARMELA* output and measured curves is reported. For clarity only

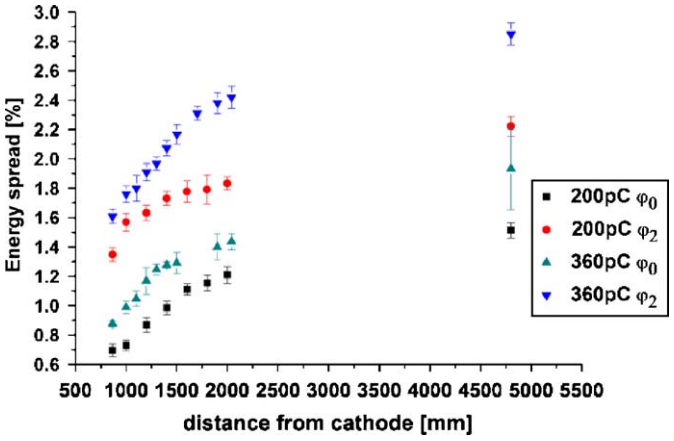

Fig. 5. Energy spread measurements as function of distance from cathode. Four different situations have been explored.

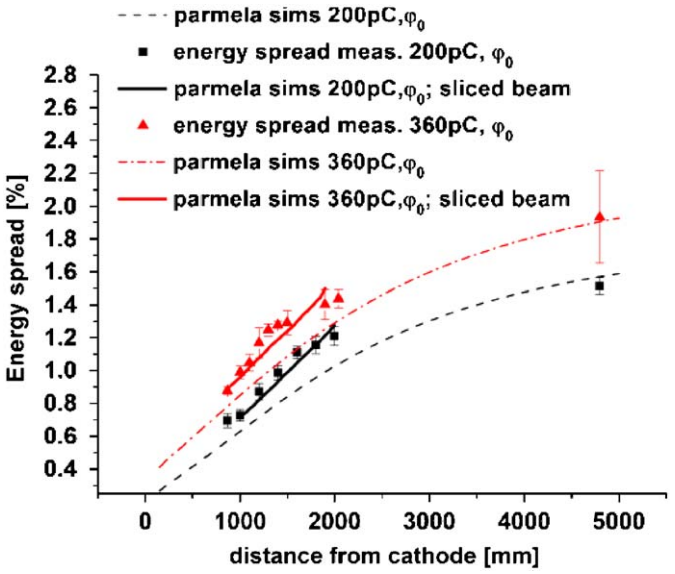

Fig. 6. Comparison between simulations and measurements in two experimental situations extracted from the data of Fig. 5. Dashed lines represent the simulated energy spread behavior of the entire beam. Solid lines represent simulations including the beam slicing. Measured beamlet energy spread is represented by dots.

the two measurements at 200 and 360 pC of beam charge for $\phi_{inj} = \phi_0$ are shown. First of all simulations of the entire beam δE_t in the two experimental situations have been carried out to fit the last measured point (4800 mm), and reported by dashed lines in Fig. 6. The other data points happen to be always above the simulated curves. In order to fit them a simulation of the entire procedure, simulating also the beam slicing, is needed. The *RMS* energy spread of the resulting particle distribution has been plotted using solid lines in Fig. 6. The simulations agree with the experimental data, showing that, although δE_b reproduces the relative behavior of the full beam evolution, there is a significant difference in the absolute values, typically with $\delta E_b > \delta E_t$.

One first information that one can retrieve from measurement-simulations comparison is that wakefields seen by the beam along the transport channel and caused by the e-meter corrugated structure (the three bellows forming the emittance-meter device) give a negligible energy spread rise. *PARMELA* indeed does not take into account wakefields of such a structure. These measurements validate analytical calculations and simulations about wake effects on the beam along the corrugated structure [16].

Moreover from the recorded image data at the spectrometer screen the full energy distribution can be studied, by projecting the beam image onto the horizontal axis which is linearly correlated with energy (by an horizontal non-zero dispersion).

In Fig. 7 the results of the comparison between measured and simulated beam spectra are displayed. The raw images are also shown. The collimating slit always selects the central part of the beam (maximum energy spread). The first three columns show the beamlet energy distributions after the collimation in different positions (100, 140 and 200 cm); the last column is relative to the full beam at the spectrometer screen with no collimation. The simulated energy profiles can be understood taking into account the experimental laser beam shape (Fig. 8). As confirmed by simulations, the double horn structure on the electron distribution is linked to the presence of two separate peaks on the initial distribution. Decreasing the peak separation, or decreasing the relative amplitude difference between peaks and the central value, has the effect of changing the structure in the beamlet spectrum. This is due to the effect of the longitudinal

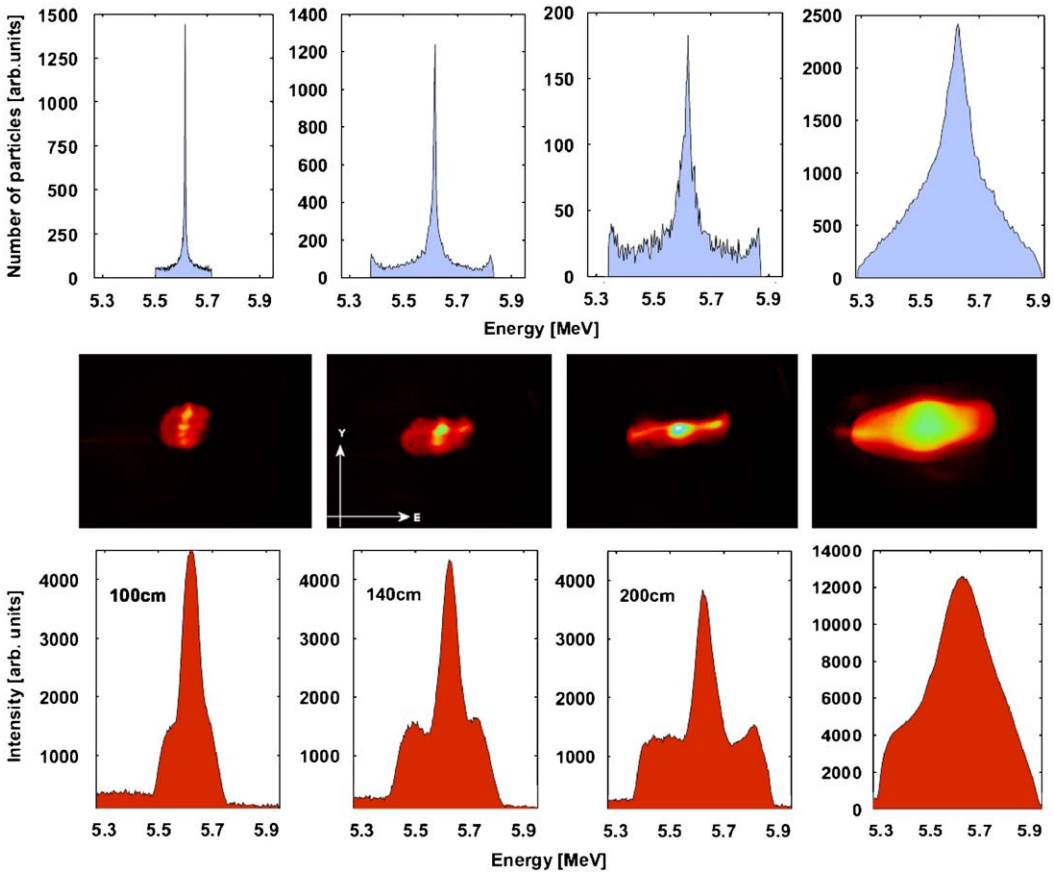

Fig. 7. *Upper row*: simulated energy profiles at 100, 140, 200 and 480 cm (spectrometer screen) from cathode plane; *middle row*: relative experimental data images at the spectrometer screen (horizontal axis being the dispersion axis). The first three images are taken by slicing the beam at different z positions along the propagation axis: 100, 140 and 200 cm; the last one is the spectrum of the whole beam at 480 cm; *lower row*: horizontal profiles of the data images (middle row).

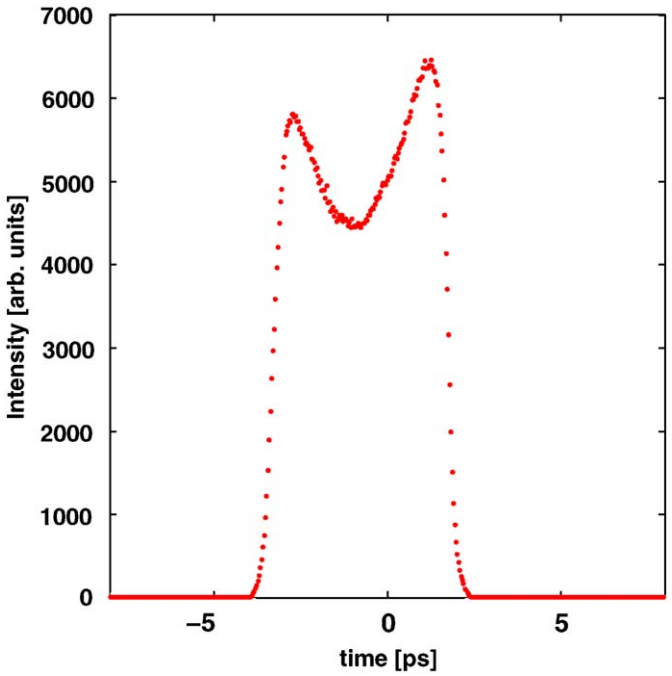

Fig. 8. Measured laser longitudinal profile.

space charge forces on the longitudinal phase space distribution. Space charge fields transform density modulations into energy modulations. The initial density modulation derives from the laser pulse time structure modulation. This temporal modulation is then transferred to energy by the self-field action, which moves particles toward a more homogeneous charge distribution.

The full width and the shape of the measured energy profile are reproduced with good accuracy by simulations. Few considerations stem from Fig. 7: the first three columns clearly show the development (both in the simulations and in the experiment) of the double horn structure in the spectrum. Nevertheless the spectrum of the full beam (last column of the graph) does not show this shape, both in measurements and in simulations, meaning that without the collimator it would not be possible to directly correlate the electron beam energy profile to the laser longitudinal profile.

Longitudinal space charge (LSP) forces strongly depend on the beam longitudinal shape, and they are the only source of energy spread alternative to RF field variation for inner particles, i.e. close to the beam transverse centroid. On the other hand moving away from the beam barycenter the presence of other sources of energy variation across the bunch tends to wash out the energy modulation induced by the LSP. For example, the RF accelerating fields as well as longitudinal space charge fields depend also on transverse coordinates, i.e. particles at different distances from the center will experience different gradients. This can be better understood looking at Fig. 9. It shows a comparison between simulated $\phi-E$ and $X-E$ planes for the measured beam at the collimator entrance (left column), and at the exit (right column). The shaded area on the lower-left plot simulates the action of the collimator. Paying attention to the two lower plots, it is clear as the correlation between X and E in case of the entire beam changes with X effectively blurring the longitudinal structure. By

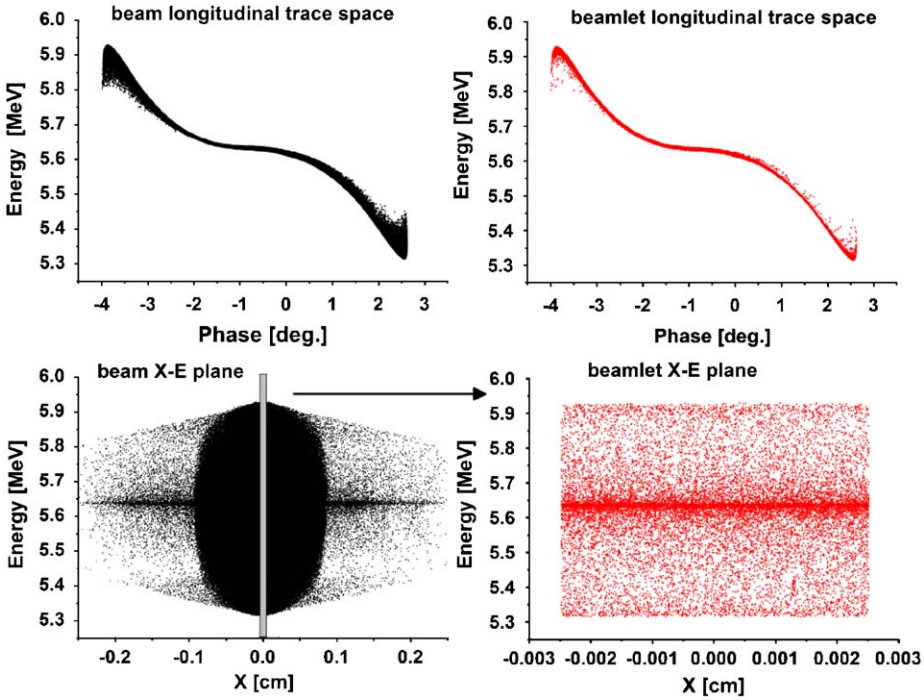

Fig. 9. Comparison between simulated $\phi-E$ (upper row) and $X-E$ (lower row) planes for beam used in measurements; on the left column (graphs with black dots) the entire beam at 140 cm downstream the cathode; the right column (red dotted graphs) represents the two planes just after the collimator (represented on the lower-left graph by the gray rectangle). (For interpretation of the references to color in this figure legend, the reader is referred to the web version of this article.)

slicing transversely a laminar beam (with a small aperture, compared to the transverse beam size) in a region close to the transverse center of mass selects particles whose energy differences are mainly due to longitudinal effects. The result is that of eliminating the correlation between X and E of the remaining beam (lower-left plot of Fig. 9).

In our case the sampling is only applied along one direction (single slit collimator), so that the remaining particles preserve a dependence from the other transverse coordinate. A round collimator with a small radius would be used to maximize the longitudinal self-field contribution, but the one-dimensional cut is enough to make this correlation emerge from data.

5. Experimental observation of longitudinal and transverse plane correlations

Another observed phenomenon is the presence of double peaked profiles in beamlet images at the imaging screen. As an example in Fig. 10 is reported one particular beamlet image, and its profile integrated along the cutting direction.

The laser beam had a Gaussian longitudinal profile, with 10 ps *FWHM* duration. The situation has been changed from the previous one since we want to observe this phenomena in a well-known dynamical situation.

The collimator position was fixed at the emittance minimum point, where the double peak structure turned out to be more evident. Beam charge was 1 nC and the optimum injection phase was 12° off the minimum energy spread (ϕ_2), resulting in a non-optimized energy spread. A first qualitative observation of the beamlet image already reveals some features: one of the two subsets is more dense and focalized while the second one (below) is dilute along the horizontal axis. The integrated profile (right graph of Fig. 10) shows a net separation between the two peak centroids.

Fig. 11 reports the result of a centroid analysis on a full set of data, corresponding to an emittance measurement, taken by moving transversely the slits along the beam with a step of $\sigma_{beam}/2$: all the images collected have been analyzed to fit separately the centroid value of the two beam spots; these centroids have then been plotted versus the transverse position of the slit. Squares in the graph represent the positions of the slit (proportional to the abscissa), circles report the calculated centroid of the more focalized structure (primary beam) while triangles those of the dilute structure (secondary beam). The difference between circles/triangles and square symbols divided by the distance between the slit mask and the imaging screen gives the beamlet mean divergence. A beamlet with zero mean divergence should have the distribution centered on the relative square symbol. Circles and triangles represent centroids of differently behaving beams: one (circles) is still slightly converging, while the other one (triangles) is already strongly diverging.

The reconstructed trace space [17] relative to such emittance measurement is reported in the left plot of Fig. 12. It shows a particular shape that recalls, as expected, the centroid distribution of Fig. 11: two separate branches with different angles with respect to the x, x' axes result in a characteristic X-shaped picture. The simulation of the measurement reported on the right of Fig. 12 underlines the energy dependence: particles belonging to different trace space populations have also different momentum, implying a correlation between the different divergences and the spread in energies. Particles in the small secondary divergent beam have lower energies.

To clarify the role of energy spread on the transverse dynamics, we experimentally characterized this behavior collecting data for different injection phases. In Fig. 13 the beam is sliced by the slit aperture (fixed at $1.5 \times \sigma_{beam}$ off center) while the launch phase is varied by 12°, starting from the minimum energy spread phase ϕ_0 to ϕ_2.

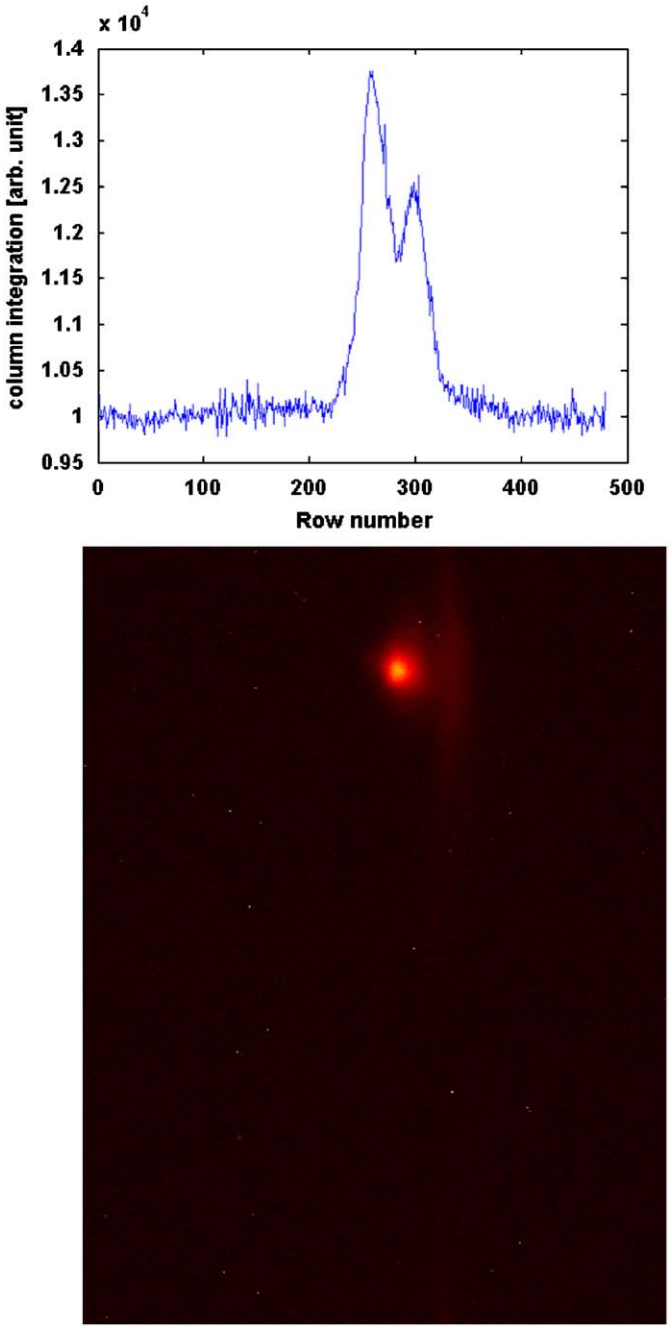

Fig. 10. Bottom: (1) a sliced beam on the screen during an emittance measurement; two separate beamlets are visible. Top: (2) relative image profile obtained integrating the picture over the columns.

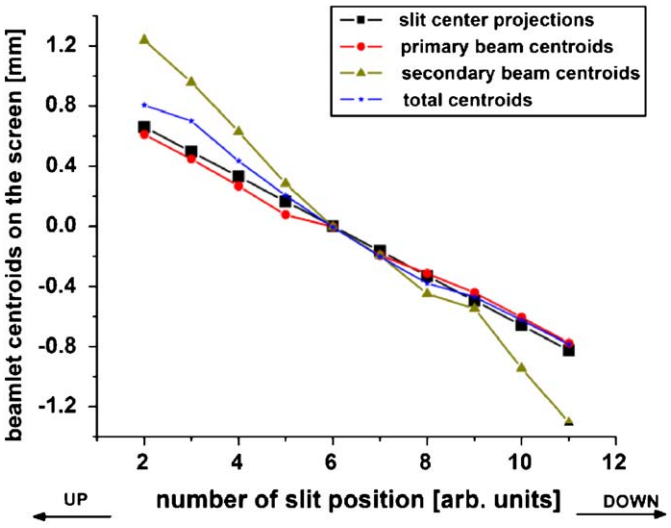

Fig. 11. Plot of different beamlet centroids; the beam at 140 cm from cathode was sliced along vertical direction, in 13 different positions. The first position (1) is the upper one. In the first (1) and the last two positions (12, 13) there was no signal found.

The growth of a secondary beam completely separated from the primary one is observed, correlated to the increase of the energy spread. The charge migration between the two beamlets (from left to right pictures of Fig. 13) corresponds to a charge exchange between the two branches of the *X*-shaped trace space. The same procedure has been repeated at the spectrometer screen to reveal the energy difference between the two beams to allow a comparison with the simulations. The results are reported in Fig. 14. The quadrupole doublet before the dispersive section has the effect of magnifying the vertical separation between the two distributions because of the vertical off-axis dipolar component in the quadrupole magnet. The horizontal axis in the figure is the dispersion plane and so it is proportional to the beam energy with higher energy on the right, and the injection phase values are the same as used in Fig. 13.

Confirming the simulation results, the difference in mean energy between the main beamlet and the growing secondary beamlet distributions is about 4%, with a primary beamlet mean energy of 5.65 MeV. The secondary beamlet contains only particles with lower energies ($E_{mean} = 5.43$ MeV).

In order to get a deeper understanding of this significant correlation, let us look at the simulated $X-\phi$ planes showing the effect of the slit mask collimation at the three different injection phases used during the measurements (Fig. 15). A high number of particles ($t_0 = 0.5 \times 10^6$) are used to increase the tracking resolution. A rectangle as been drawn on each plot to represent the effect of the collimator applied at $1.5 \times \sigma_{beam}$ off center; the particles have been tracked 140 cm from cathode; the particle energy is encoded in the color map.

We note how particles in the tails behave totally differently than the beam core, with transverse beam sizes that do not follow the smooth variable envelope of the central region. Moreover the number of particles in the beam tails increases moving away from the optimum injection phase. At $\phi = \phi_0$ the number of such particles is very small (about 0.5%, left plot of Fig. 15) and not visible in practical measurements. Moving toward $\phi = \phi_2$, the charge fraction in the tails increases, from 1% of the beam charge (ϕ_1, middle plot of Fig. 15), to about 10% (ϕ_2, right plot of Fig. 15).

What is interesting here is the net separation of the two particle subset that leads to separate beams. The beam itself has a double peaked distribution in divergencies, which does not have a correspondence in the energy distribution (that has a smooth profile). This behavior reveals the presence of some threshold phenomena dividing particles into two subsets with different transverse dynamics, deciding on the base of their energy and longitudinal position along the bunch.

Carlsten [7] and Anderson [18] already pointed out theoretically the origin of the bifurcation in beam dynamics which corresponds to the measured *X*-shaped trace space. This is basically due to the tradeoff between focusing external magnetic force and internal self-forces. All together energy, energy spread and bunch longitudinal density determine which fraction of the beam will rotate clockwise in trace space (crossover) and which

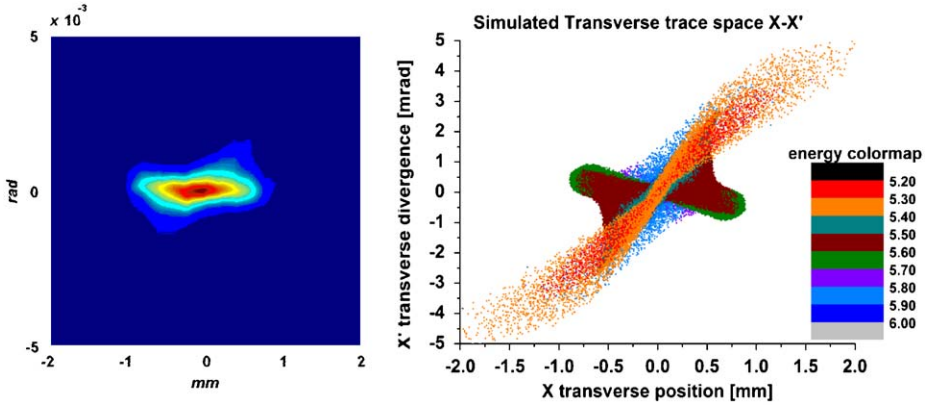

Fig. 12. On the left, transverse trace space reconstructed from measurements (same dataset used for Figs. 10 and 11). On the right: simulation of the measurement using *PARMELA* code; a colormap is used to highlight different particle energies.

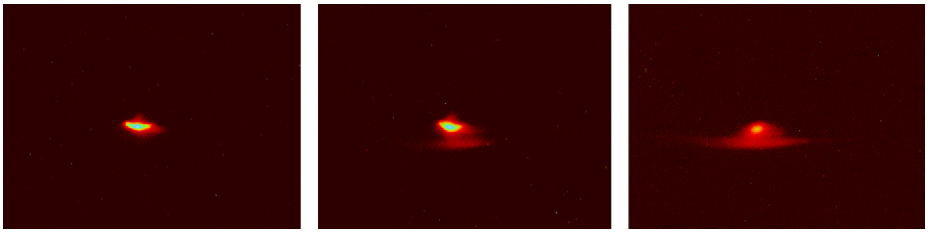

Fig. 13. Beamlet images on the imaging screen, for three different phases; from left: ϕ_0, ϕ_1, ϕ_2.

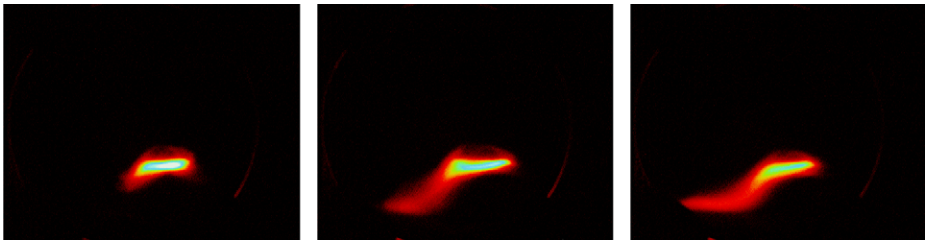

Fig. 14. Beamlet images at the spectrometer screen for three different phases (same conditions of Fig. 13).

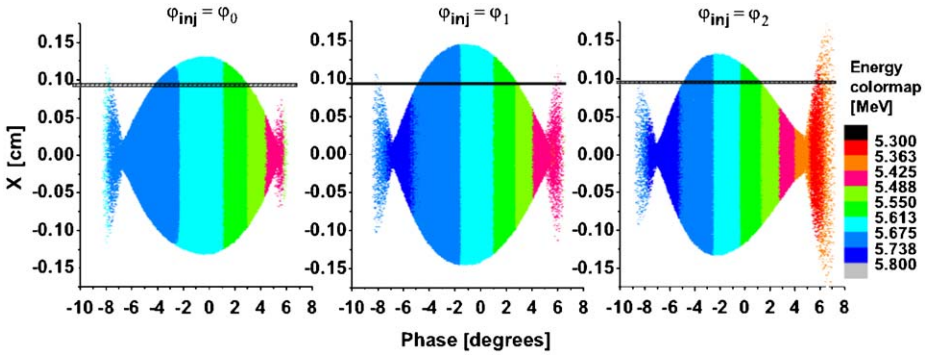

Fig. 15. Simulated $X-\phi$ plane for three different phases (same as measurements); the same colormap scale has been used for each plot, outlining different particle energies.

one will instead go through a space charge dominated waist (counterclockwise rotation). Particles belonging to bunch regions (slices) with low charge densities experience weak self-forces defocusing fields and will evolve mostly following the single particle dynamics, i.e. passing from convergent to divergent by crossing the X' axis (clockwise rotation). On the other hand, high density slices undergo a space charge dominated dynamics. Their flow will be quasi-laminar, with a decrease of their transverse momenta as the beam approaches the waist position and consequently a counterclockwise rotation in the transverse trace space. The joint work of RF and space charge forces in the gun gives to the beam an energy–time correlation, with higher and lower energy particles located in the tails of the longitudinal distribution. The beam extremities (both in energy and in time)

have thus a lower charge density than the core and form, as stated above, the secondary beam.

The explanation of why in the experimental data we observe the low energy tail, but not the high energy tail, is also given in Fig. 15. The reason is to be found in the energy dependence of the electron magnetic rigidity: between two different longitudinal beam slices (head and tail of the beam) with equal plasma frequency ω_p [7] the one with lower mean energy undergoes a more dramatic emittance-dominated crossover, due to the stronger focalization by the magnetic lens. An off-axis slit mask intercepts almost all of the low energy particles and none of the high energy ones.

As clearly appears from trace spaces reconstructions, the presence of the secondary beam strongly increases the beam emittance, and the fraction of the beam belonging to it should be minimized. Since the evolution of this portion of the beam is emittance-dominated, the compensation process does not hold, and the presence of the high solenoidal magnetic fields required to control the denser beam core leads to an explosion of the head and the tail of the beam, making the overall projected emittance much higher than the optimum achievable.

Furthermore for FEL application, the transverse emittance of the head and the tail of the beam is such that they do not contribute to the FEL amplification process. This effect can lead to a projected beam transverse emittance value dominated by this two small parts of the beam.

An idea to better characterize the performance of a beam in a FEL machine would be that of take into account this effect with the use of two different parameters: the first one describing the relative fraction of the beam that stays in the emittance-dominated tails, and the other one measuring the core transverse emittance, where the core is defined as the space charge dominated part of the beam. Both parameters should be minimized at the same time to achieve best performances.

6. Conclusions

A method for measurement of correlated energy spread of a beam as a function of distance from photo-injector cathode has been discussed. It makes use of the emittance-meter tool to slice the electron beam and freeze its energy distribution at a known propagation distance from the cathode. The proposed method can be used to calculate the evolution of the rms value of the energy distribution, and make systematic studies of its behavior as a function of charge density, RF phase and magnetic focusing force. First tests on the SPARC photo-injector demonstrate the feasibility of the measurement. The central beamlet energy spread has been measured, and the agreement with the simulations points out the validity of the procedure.

A deeper look to the energy profile of the central slice reveals correlations with the initial longitudinal beam profile; in the presented case, the presence of a double peaked laser longitudinal profile leads to a double peaked electron beam energy distribution. When measuring the entire beam this correlation is smoothed by the integration over different transverse positions that experience different self-force fields.

Finally, the correlation between longitudinal and transverse planes has been investigated, relating the double peaked beamlet transverse profile found in measurements to the bifurcation of transverse trace space, and this bifurcation to the different tradeoff between self- and applied field of the various beam longitudinal slices. The energy and density spread in the beam, together with the presence of a chromatic focusing element along the transport, leads to a separation of the beam into two different dynamical regimes (“crossover” and “space charge dominated”). The energy dependence of such a behavior inside a single bunched beam has been experimentally observed, and the procedure can be used as a qualitative tool to evaluate the charge ratio between the two trace space branches.

Acknowledgments

The authors wish to thank all SPARC collaboration scientists and engineers who contributed to the design and commissioning of the SPARC machine and to the emittance-meter construction. Special thanks to V. Lollo for his contribution to the system mechanical design, engineering, and bench testing, F. Anelli and S. Fioravanti for their work on motor controllers. Also thanks to A. Battisti, L. Cacciotti, R. Sorchetti, L. Antonio Rossi and S. Stabioli.

References

[1] M.J. Hogan, C. Pellegrini, J. Rosenzweig, S. Anderson, P. Frigola, A. Tremaine, C. Fortgang, D.C. Nguyen, R.L. Sheffield, J. Kinross-Wright, A. Varfolomeev, S. Tolmachev, R. Carr, Phys. Rev. Lett. 81 (1998) 4867.
[2] M. Babzien, I. Ben-Zvi, P. Catravas, J.-M. Fang, T.C. Marshall, X.J. Wang, J.S. Wurtele, V. Yakimenko, L.H. Yu, Phys. Rev. E 57 (1998) 6093.
[3] V. Ayvazyan, N. Baboi, et al., Phys. Rev. Lett. 88 (2002) 104802.
[4] A.M. Tremaine, S.G. Anderson, et al., Particle Accelerator Conference, Knoxville, Tennessee, 2005, pp. 1464–1466.
[5] X. Dao, S.-J. Park, I.-S. Ko, X.J. Wang, H. Ihee, Particle Accelerator Conference, Knoxville, Tennessee, 2005, pp. 3721–3723.
[6] K.-J. Kim, Nucl. Instr. and Meth. A 275 (1989) 201.
[7] B.E. Carlsten, Nucl. Instr. and Meth. A 285 (1989) 311.
[8] L. Serafini, J.B. Rosenzweig, Phys. Rev. E 55 (1997) 7565.
[9] M. Ferrario, M. Boscolo, V. Fusco, C. Vaccarezza, C. Ronsivalle, J.B. Rosenzweig, L. Serafini, The Physics and Application of High Brightness Electron Beam, World Scientific, Chia Laguna, Sardinia, 2002.
[10] M. Ferrario, et al., Phys. Rev. Lett. 99 (2007) 234801.
[11] S. Cialdi, M. Petrarca, C. Vicario, Optics Lett. 31 (2006) 2885.
[12] L. Catani, A. Cianchi, E. Chiadroni, S. Tazzari, M. Boscolo, M. Castellano, G. Di Pirro, D. Filippetto, V. Fusco, L. Palumbo, et al., Rev. Sci. Instrum. 77 (2006) 93301.
[13] A. Cianchi, et al., Phys. Rev. ST Accel. Beams 11 (2008) 032801.
[14] L. Serafini, IEEE Trans. Plasma Sci. 24 (2) (1996).
[15] L.M. Young, Los Alamos National Laboratory Report, LA-UR-96-1835.
[16] V. Fusco, Ph.D. Thesis, University “LA SAPIENZA” of Rome, 2004, unpublished.
[17] D. Filippetto, Sparc Note, SPARC/EBD-07/002 ⟨http://www.lnf.infn.it/⟩.
[18] S. Anderson, Ph.D. Thesis, UCLA, 2002.